Pergamon

Int. J. Heat Mass Transfer. Vol. 39, No. 16, pp. 3497–3509, 1996

0017–9310/96 $15.00+0.00

PII: S0017–9310(96)00004–X

Visualization of natural convection in a side-heated cavity: transition to the final steady state

W. SCHÖPF and J. C. PATTERSON

Centre for Water Research, University of Western Australia, Nedlands, WA 6009, Australia

(*Received* 23 *May* 1995)

Abstract—The flow evolving in a water-filled square cavity which is suddenly heated and cooled on the opposing sidewalls is observed by using the shadowgraph technique. The horizontal boundaries of the cavity are thermally insulating, while the heated and cooled vertical sidewalls are conducting. In a previous publication, the emphasis was on the very early stages of the flow development. As part of this initial evolution, two travelling wave groups were observed. The present paper continues the description of the flow development until a steady state is reached. A clear visualization of the interaction between the second wave group and the laminar intrusion flow across the roof of the cavity is given. The subsequent decay of the horizontal intrusion triggering the thermal stratification in the cavity core and the adjustment of the vertical boundary layer are also observed. The final state is characterized by waves which continuously travel along the boundary layers. Copyright © 1996 Elsevier Science Ltd.

1. INTRODUCTION AND BACKGROUND

When a fluid-filled rectangular cavity is differentially heated and cooled from the opposing sidewalls, a complex flow develops. This is one of the classical heat and mass transfer problems with significance for fundamental fluid mechanics, as well as for engineering and geophysical applications. Industrial cooling systems, crystal growth procedures, building insulation and buoyancy-induced horizontal mass transfer in geophysical flows all fall into this category. In many of these applications, the imposition of the horizontal temperature gradient is time-dependent, therefore an understanding of both the temporal development of the flow and of the corresponding heat transfer properties is as equally important, as is the investigation of the final steady state. Most of the more recent research, both experimentally and numerically, has been focused on either the transient start-up flow following the sudden heating and cooling of the sidewalls [1–9], or the transition from laminar to time-dependent flow and the route to chaos [10–15].

The experimental system under consideration is that of an initially isothermal and motionless fluid, which is contained in a square cavity with thermally conducting vertical sidewalls and insulating top and bottom boundaries. The flow is started by suddenly raising and lowering the temperatures of the opposing sidewalls by the same amount ΔT, and then maintaining those temperatures. The evolving flow consists of narrow vertical boundary layers adjacent to the heated and cooled walls, which exit into horizontal intrusions travelling across the roof and floor of the cavity before meeting with the opposing wall boundary layers. The complex interactions between the incoming intrusions and the receiving boundary layers establish the means by which the core region of the cavity stratifies. For a sufficiently low Rayleigh number, a laminar time-independent flow is eventually achieved. At a higher Rayleigh number, however, a time-periodic flow may result, or if the Rayleigh number is sufficiently high, the flow becomes turbulent (for a further discussion, see ref. [1]).

Among the many phases of the flow development from the motionless and isothermal condition to one characterized by a variety of length and velocity scales, one particularly striking sequence of events in the early part of the flow has attracted a great deal of recent attention. That is the presence of two separate groups of short-lived travelling waves observed on both the vertical boundary layers and the intrusion flows. The first group of waves follows start-up, and the second group emerges from the first interaction between the incoming intrusion and the opposing boundary layer. The presence of these waves was identified from experimental and numerical observations [5–9, 16]. Of additional interest are the horizontal intrusion flows, which also show some striking characteristics. One is a complex flow separation near the exit from the vertical boundary layer after the flow has become established. There has been an extensive discussion about the nature of this flow divergence, but no unambiguous explanation has yet been provided (see e.g. refs [3–5, 7, 12, 17]). Another one is the interaction between the intrusion flow and the vertical boundary layer, especially how the impact of the two travelling-wave groups lead to complete changes in the intrusion behaviour [5, 6, 9]. Finally, the intrusions show a strong similarity to classical gravity currents (for the latter, see e.g. ref. [18]), and a possible connection has been discussed recently [9].

The experimental investigations mentioned above

NOMENCLATURE

d	thickness of isothermal fluid layer
g	acceleration due to gravity
g'	reduced gravity, $g\Delta\rho/\rho_0$
h	height and width of the cavity
Pr	Prandtl number, ν/κ
Ra	Rayleigh number, $g\alpha h^3\Delta T/\nu\kappa$
t	time
T	period of internal waves
T_0	ambient temperature
ΔT	temperature difference between ambient and one wall
ΔT_i	temperature difference between ambient and intrusion
v	wave velocity
x	horizontal distance from the bottom left corner
y	vertical distance from the bottom left corner.

Greek symbols

α	coefficient of thermal expansion
κ	thermal diffusivity
ν	kinematic viscosity
ρ_0	mean density of the working fluid
$\Delta\rho$	density difference between ambient and intrusion.

Subscripts

1,2	fluid layer 1 and 2
s1, s2,...,s30	steady-state waves 1, 2, ..., 30

could confirm the features of interest only indirectly. Evidence of the travelling waves for example was given by isolated temperature measurements using thermistors which were placed inside the hot vertical boundary layer and in the top horizontal intrusion [6, 8]. From these temperature time series taken at one or more fixed locations, only localized properties could be obtained. Since the properties of the waves and especially of the intrusion alter as they move downstream [7, 16], their true character is only revealed when using many sampling locations. However, the number of thermistors is usually restricted to about five to 10. The visualization techniques used in refs. [3, 6, 8] could reveal an overall picture of the large-scale flow field, but the timing for the streak photographs was not appropriate for resolving the relatively fast travelling waves and the spatial resolution was not fine enough to characterize the intrusion flow.

To overcome those problems, we have used the shadowgraph technique as a means of flow visualization. Rather than yielding temperature time series only at specific locations, the shadowgraph images give an overall (two-dimensional) map of the temperature signal. Although for our experiment this technique cannot be used as a tool for quantitative temperature measurements, its high quality has helped identify new and unexpected flow features.

In a previous publication [9], we have applied this method to the first stages immediately following the flow initiation. For the first time, the two groups of travelling waves could be made visible and followed through their journey along the boundary layer. Probably the most striking result was the visualization of the intrusion flow, revealing a strong similarity with gravity currents, even though the intrusion is stratified and formed in a different way to the classical gravity current experiments. Some of the features of the intrusion predicted by numerical simulations and streak photographs, such as the region of flow separation, were confirmed with greater clarity than previously. Also a clear picture of the interaction between the first group of waves and the intrusion was given. Additionally, some new features such as the distinct temperature structures inside the intrusion head were identified. Previously measured temperature signals in this region have been interpreted as the remnants of the boundary-layer waves [6, 8], however, according to our measurements there is no clear connection between these two features.

For a typical temperature difference ΔT of about 4 K (between one wall and the ambient), this first phase of the flow development is over after about 2 min. In this paper, we continue the description of the flow evolution by covering a much larger time frame until a steady state showing no further qualitative changes is reached. In Section 2, we discuss the experimental setup including the optics and the shadowgraph technique. In order to define a starting point, we briefly address the second group of travelling waves, and the established intrusion prior to the impact of these waves. The new results are then presented and discussed in three steps: Section 3 deals with the interaction between the second group of waves and the intrusion; the decay of the intrusion triggering the core stratification and the subsequent change of the vertical boundary layer are the topics of Section 4; and the final state which is characterized by continuously travelling waves along the vertical boundary layers is described in Section 5. We conclude the paper with some outlooks and motivations in Section 6. We would like to emphasize that, like ref. [9], the present paper is of observational nature and reports in a qualitative way the development of a transient flow which is remarkably rich in features. Quantitative models for the underlying physics controlling these features

are in many cases not available at this stage, and are beyond the scope of this paper.

2. EXPERIMENTAL SETUP

2.1. *Experimental tank and fluid properties*

The experimental system of interest is that of an initially motionless Newtonian fluid, which is contained in a square cavity of height and width h and held at the ambient temperature T_0. The horizontal upper and lower boundaries are thermally insulating, while the vertical sidewalls are assumed to be perfect heat conductors. The flow is initiated by suddenly changing the temperatures of the opposing sidewalls from T_0 to $T_0+\Delta T$ and $T_0-\Delta T$, respectively. The flow is assumed to be two-dimensional with the relevant coordinates being x in the horizontal and y in the vertical direction, and the origin lying in the lower hot corner. The nondimensional parameters describing this problem are the Rayleigh number and the Prandtl number:

$$Ra=\frac{g\alpha h^3\Delta T}{\kappa\nu},\quad Pr=\frac{\nu}{\kappa},\tag{1}$$

where g is the acceleration due to gravity and α, ν and κ are, respectively, the coefficient of thermal expansion, the kinematic viscosity and the thermal diffusivity of the fluid. For a rectangular, nonsquare cavity, another relevant parameter would be the aspect ratio.

The experimental rig is that described in ref. [6] with some improvements according to ref. [9], therefore only a brief description is given. The cavity containing the working fluid is constructed from perspex in order to model the insulating boundary conditions, except for the conducting sidewalls which are made from copper of thickness 1 mm. The size of the two-dimensional working region is 24×24 cm and the extent in the third dimension is 50 cm. Adjacent to each copper wall is a large reservoir containing heated and cooled water, which, respectively, are maintained at the desired temperatures of the hot and cold walls. These reservoirs are separated from the copper walls by removable gates and an air gap. Upon initiation, the gates are raised simultaneously in order to provide a sudden thermal contact between the heated and cooled water and the copper walls, thus leading to the desired step change in the thermal boundary condition.

The experiments reported here have been carried out with water as the working fluid. The mean temperatures ranged from $T_0=20.4$ to 20.8°C, giving Prandtl numbers between $Pr=7.0$ and 6.9. The temperature differences between the vertical sidewalls and T_0 usually ranged from $\Delta T=3.2$ to 3.5 K corresponding to Rayleigh numbers between $Ra=6.9\times10^8$ and 7.3×10^8, except for one experiment, where $\Delta T=2.35$ K corresponding to $Ra=4.9\times10^8$. The respective values are given below when the individual measurements are discussed.

2.2. *Optical setup and shadowgraph technique*

Since the flow is driven by temperature gradients inside the fluid, the well-known shadowgraph technique is best-suited for visualization purposes. A general discussion is given in ref. [19], for various applications see e.g. refs. [20–22], and especially for the system considered here see ref. [9]. The principles are rather simple: the temperature variations with space and/or time inside the fluid lead to a modulation of the refractive index of the fluid, which in turn leads to deflections of the incoming parallel light beam. Therefore, the distribution of the light intensity in the shadowgraph image is a representation of the spatial temperature field inside the fluid, while a time series of images can reveal its temporal evolution.

The optical setup is the same as used in ref. [9] and is sketched in Fig. 1. A point light source is generated by placing a pinhole in front of a halogen lamp. The light is made parallel by means of a spherical mirror, which has a diameter of 30 cm and a focal length of about 2.4 m. The resulting parallel light beam shines through the experimental tank in such a way that the two-dimensional working region is illuminated. A second mirror, which is identical to the first one, converges the transmitted light at a CCD-camera, leading to the Z-shaped setup shown in Fig. 1. As has been discussed in ref. [9], in our experiment this method cannot be used for a quantitative measurement of the temperature field, however, the resulting images are very good qualitative representations of the temperature field yielding a very high quality of flow visualization (see Fig. 2). In cases where the heat transport is mainly by convection rather than by conduction, the shadowgraph images are also a very good representation of the velocity field in the fluid.

The pictures taken by the black-and-white CCD-camera are digitized by a frame-grabber board implemented in a PC/AT-80486 computer. This procedure results in individual images consisting of arrays of 512×512 pixels of 8-bit grey-scale values, which are stored on the computer hard disk for further processing. The time elapsed between consecutive pictures is very accurately determined by a quartz-oscillator and varies from experiment to experiment. Alternatively, the whole flow evolution as seen by the shadowgraph method can be recorded for further inspection on tape by a videorecorder.

2.3. *Examples of shadowgraph images*

Due to the diameter of the spherical mirrors (30 cm), it is not possible to display the whole working region with its diagonal dimension of 34 cm. Therefore, we will use only a little more than the heated half, a typical example of which is shown in Fig. 2. Here, the temperature difference is $\Delta T=3.5$ K corresponding to $Ra=7.2\times10^8$. This particular image is taken 106.92 s after start-up, just before the first wave of the second group hits the top intrusion. The hot vertical wall is to the left with the bright line representing the inner edge of the boundary layer. The

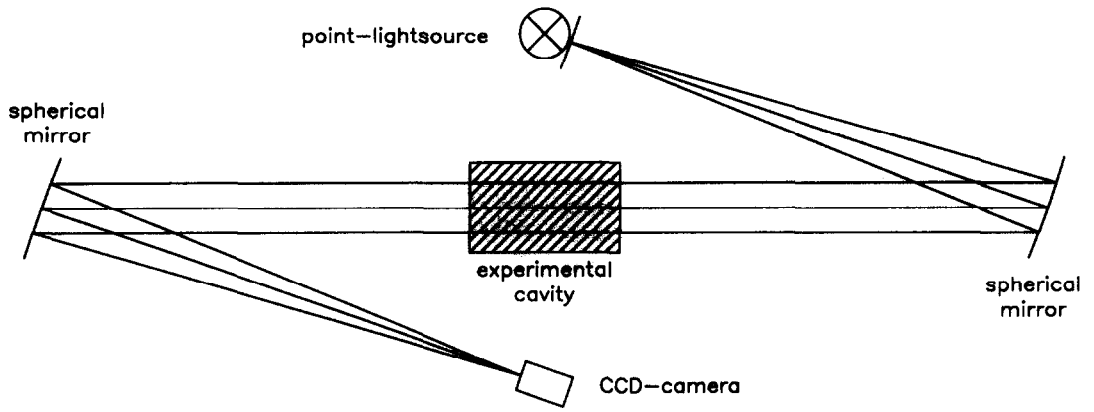

Fig. 1. Schematic layout of the optical setup as explained in the text.

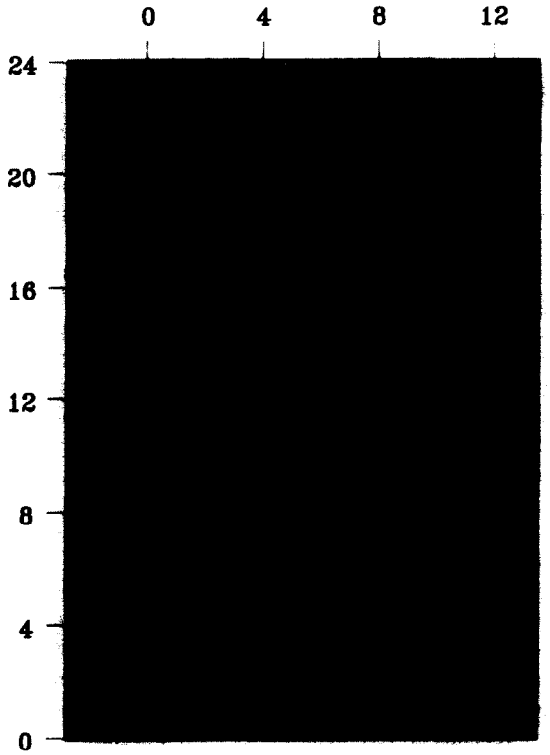

Fig. 2. Typical example of a shadowgraph image as used for composing Figs. 3–8. The Rayleigh number is $Ra = 7.2 \times 10^8$, and the image is taken 106.92 s after start-up.

origin for the system of coordinates as used throughout this paper lies in the lower left corner, with x increasing to the right and y upwards. The labels at the left-hand side and at the top in Fig. 2 and also in Figs. 3–8 indicate the distances in cm from the bottom and from the hot (left) wall, respectively.

The feature at about 16 cm up the boundary layer is the first wave of the second group, which results from the impact of the incoming cold bottom intrusion on the hot boundary layer. At this stage, after the first wave group has gone through, the intrusion flow itself is laminar. The left half of the hot intrusion is represented by the black strip along the top. A strong temperature gradient exists between this hot fluid and the colder, still isothermal, interior of the cavity and is identified by the bright line separating the intrusion from the core. The very bright feature at the top wall, about 5 cm away from the hot corner, is associated with a flow separation which is responsible for the wavy line of the intrusion (for more details, see ref. [9]). At the downstream end of the intrusion (shown at the bottom for the cold intrusion), the gradient towards the core region has weakened. The small deflection at about 7 cm up the boundary layer is the result of the 'piling up' of cold fluid as suggested in ref. [1] and further discussed in refs. [4, 6, 9]. The feature in the upper half of the picture near the right end is a small stirrer, which has been introduced into the cavity as part of the preparation for each experiment (see ref. [9]). At the top of the picture, it indicates the mid-point of the cavity corresponding to $x = 12$ cm.

For the remainder of the paper, parts of different shadowgraph images have been grouped together in form of time series. In order to introduce this kind of representation, but also to make the connection to our previous publication and to simplify further discussions, we repeat with Fig. 3 one of the figures already shown in ref. [9]. Each part shows the same narrow vertical strip (≈ 1.1 cm wide) covering the hot boundary layer, and is extracted from a full image similar to Fig. 2, each one taken at a different instant in time. The hot wall is to the left, the fluid flows from bottom to top and time increases from left to right, i.e. from Fig. 3(a) to (v). The time elapsed between consecutive pictures is 2.44 s with Fig. 3(a) taken 82.52 s and Fig. 3(v) 133.76 s after start-up. The images are taken from the same experiment as used for Fig. 2 ($\Delta T = 3.5$ K, $Ra = 7.2 \times 10^8$), and Fig. 3(k) is extracted from the same frame as Fig. 2.

The sequence shows the second group of waves travelling up the hot boundary layer and has been discussed in detail in ref. [9]. Figure 3(a) is taken prior to the impact of the bottom intrusion on the hot boundary layer and Fig. 3(v) is taken after the last of

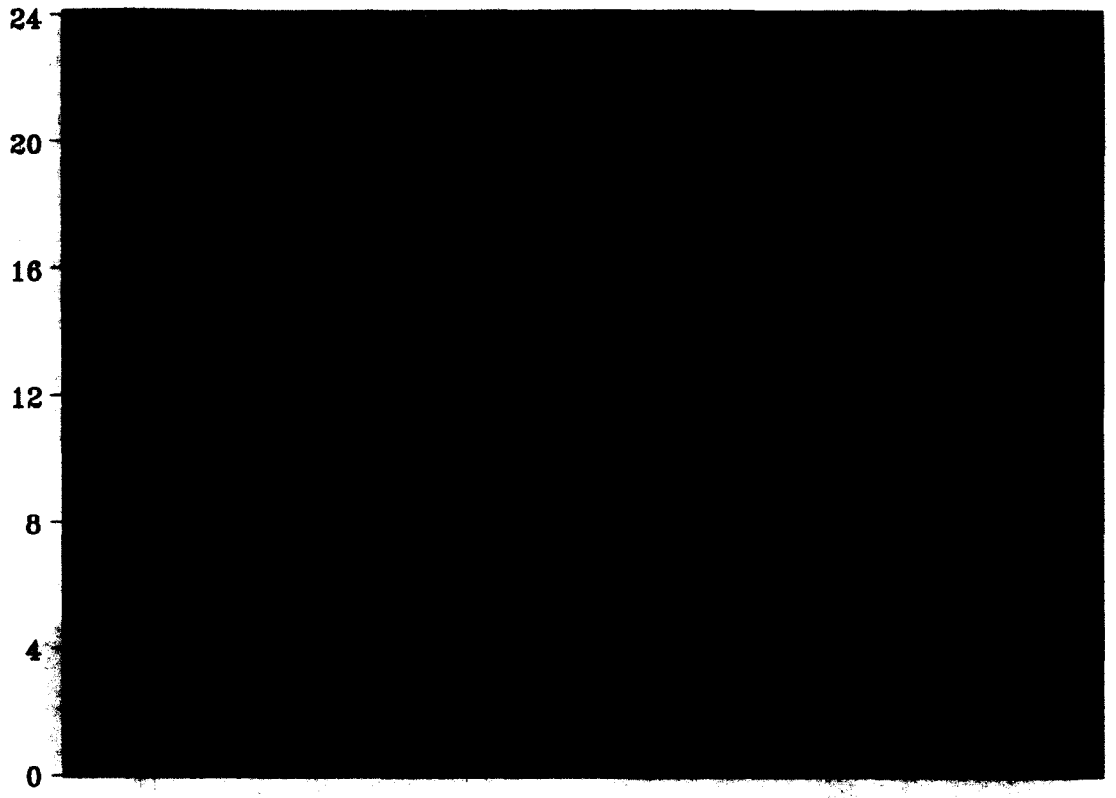

Fig. 3. Time series of shadowgraph images showing the second group of waves travelling up the hot boundary layer ($Ra = 7.2 \times 10^8$). The individual parts correspond to the following times after start-up: (a) 82.52 s, (b) 84.96 s, (c) 87.40 s, (d) 89.84 s, (e) 92.28 s, (f) 94.72 s, (g) 97.16 s, (h) 99.60 s, (i) 102.04 s, (j) 104.48 s, (k) 106.92 s, (l) 109.36 s, (m) 111.80 s, (n) 114.24 s, (o) 116.68 s, (p) 119.12 s, (q) 121.56 s, (r) 124.00 s, (s) 126.44 s, (t) 128.88 s, (u) 131.32 s, (v) 133.76 s, (after ref. [9]).

the waves has vanished into the top intrusion. There are two features of interest here. The first one is the 'piling-up' of intrusion fluid as suggested in ref. [1], which can be followed in the lower part of the picture. During impact, that part of the intrusion which interacts with the boundary layer widens as shown by the increased height of the disturbance at the bottom of the vertical boundary layer from Fig. 3(b) until Fig. 3(g), when it starts to slowly collapse back for the rest of the sequence. The second feature is the passage of the second wave group which can be seen in the upper half of the picture from Fig. 3(i–t). These waves are the result of an instability which is triggered by the impact of the cold intrusion on the (unstable) hot boundary layer.

3. INTERACTION OF THE SECOND WAVE GROUP WITH THE INTRUSION FLOW

3.1. *Observations*

In order to describe the interaction of the second group of waves with the almost steady, laminar intrusion flow and the modification of the intrusion by this impact, two different time series are used. The first one shown in Fig. 4 has a relatively poor temporal resolution, but covers the full wave group. Similar to Fig. 3, this is again a time series, but now of a horizontal strip ($\approx$3.8 cm wide) around the top intrusion. The upper part of the boundary layer can be identified at the left. Time proceeds downwards from Fig. 4(a) to (k) with 4.88 s elapsed between consecutive images. Figure 4(a) is taken 106.92 s and Fig. 4(k) 155.72 s after start-up, thus a range of about 50 s is covered. This gives a good general overview of the development from before the first wave has reached the top intrusion until the last one has passed through and disappeared. This time series is taken from the same experiment as Fig. 3 ($\Delta T = 3.5$ K, $Ra = 7.2 \times 10^8$), and Fig. 4(a) is taken from the same full frame as Fig. 3(k).

In Fig. 4(a), the visible region of the boundary layer has not yet been disturbed by the travelling waves. Their influence, however, can clearly be seen from Fig. 4(b–e). In Fig. 4(f), which is taken from the same frame as Fig. 3(u), there is no further wave activity along the boundary layer, which therefore remains almost unchanged for the remainder of the series [Fig. 4(f–k)]. Upon reaching the top corner, the waves turn around and subsequently travel along the horizontal intrusion, thereby strongly disturbing it. This is obvious from Fig. 4(c–h). By Fig. 4(c), the first wave has entered the intrusion and has created a second temperature feature alongside the already existing gradient between the intrusion and the cavity core. Every time a new wave enters the intrusion, another

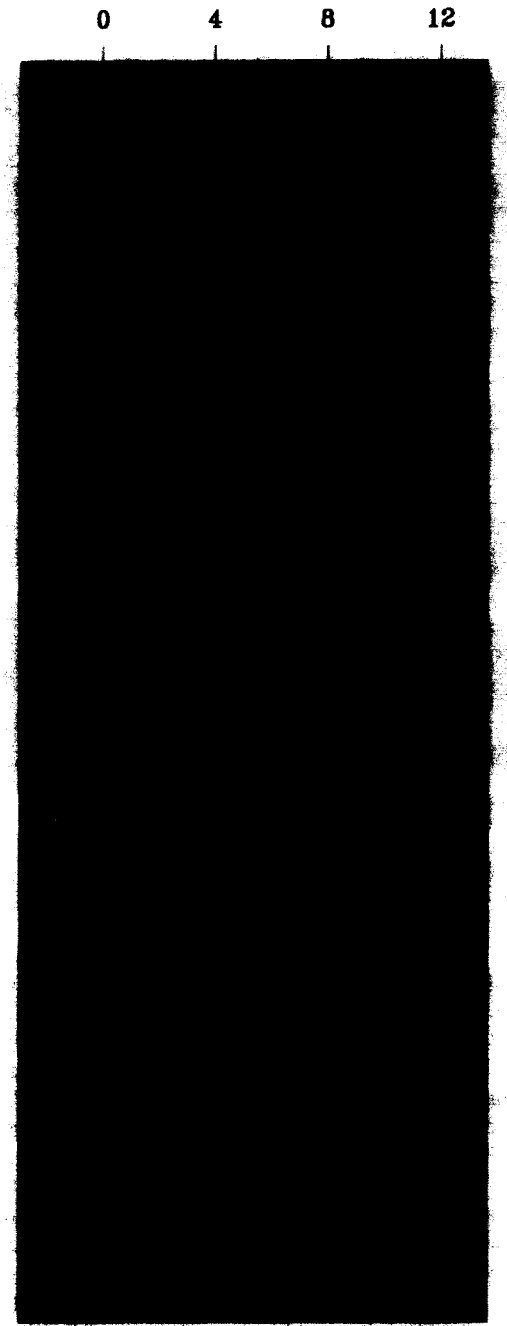

Fig. 4. Times series of shadowgraph images showing the impact of the second wave group on the top intrusion ($Ra = 7.2 \times 10^8$). The individual parts correspond to the following times after start-up: (a) 106.92 s, (b) 111.80 s, (c) 116.68 s, (d) 121.56 s, (e) 126.44 s, (f) 131.32 s, (g) 136.20 s, (h) 141.08 s, (i) 145.96 s, (j) 150.84 s, (k) 155.72 s.

such feature is created, almost splitting the original one. At first sight, the situation looks very irregular, however, it is perfectly reproducible; it is also very similar to the interaction of the first wave group with the first intrusion (see ref. [9]), but of much higher intensity. By Fig. 4(i), all the waves have travelled by, and for the rest of the time series the intrusion is again separated from the core region by a sharp gradient.

Coinciding with the impact of the waves on the intrusion is the obvious change in the separation behaviour at the top. As can be seen throughout the series, the separation point represented by the very bright feature at the top boundary slowly moves towards the left, i.e. towards the hot wall. The inflow at the top left corner steepens, making in Fig. 4(j and k) almost a complete reversal from upflow in the boundary layer to downflow in the intrusion. The downstream side of the separation point also steepens, leading to a second reversal from downflow to upflow. A third, weaker reversal turns the flow from up to down again. Neighbouring fluid regions of upflow and downflow are, respectively, separated by very strong temperature gradients which prevent the flow from travelling straight along the cavity ceiling.

The second time series shown in Fig. 5 visualizes

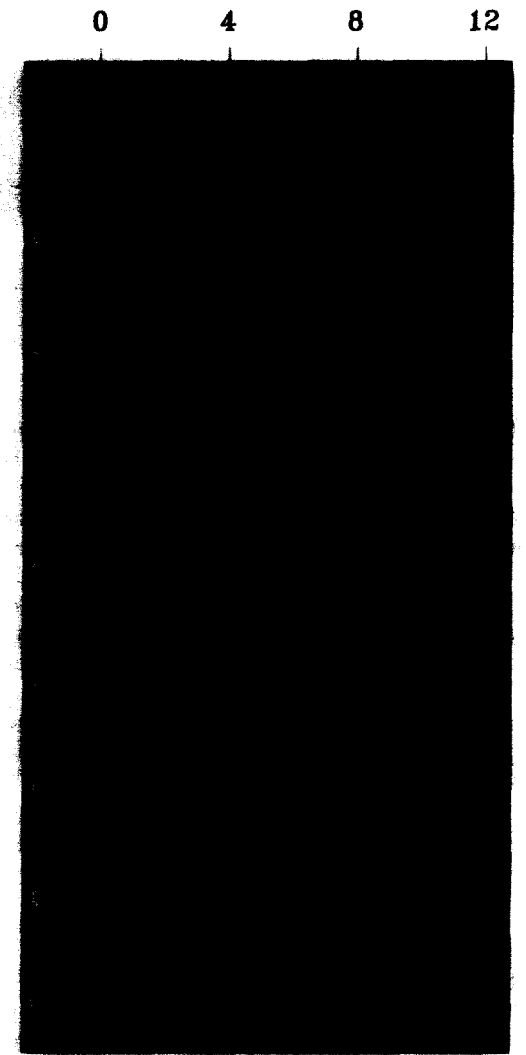

Fig. 5. Time series of shadowgraph images showing the impact of one individual wave of the second wave group on the top intrusion ($Ra = 4.9 \times 10^8$). The individual parts correspond to the following times after start-up: (a) 143.0 s, (b) 143.8 s, (c) 144.6 s, (d) 145.4 s, (e) 146.2 s, (f) 147.0 s, (g) 147.8 s, (h) 148.6 s, (i) 149.4 s.

the impact of one individual wave on the top intrusion in more detail. Again, the time series consists of the same horizontal strip around the top boundary (≈ 3.6 cm wide). The time elapsed between consecutive pictures is 0.8 s, thus yielding a much finer temporal resolution than Fig. 4. Figure 5(a) is taken 143.0 s and Fig. 5(i) 149.4 s after start-up, hence the sequence covers little more than 6 s. The images are taken from a different experiment, with $\Delta T = 2.35$ K corresponding to $Ra = 4.9 \times 10^8$. Due to the lower Rayleigh number, the structures are more regular, thus allowing an easier description, however, the behaviour is qualitatively the same for all of the experiments we carried out.

The double-gradient structure in the boundary between the intrusion and the cavity core as seen in Fig. 5(a) indicates that at least one wave has already passed by. Another wave is just coming up the boundary layer, being half-visible in Fig. 5(b) and reaching the top corner in Fig. 5(c). The double-line structure is typical for these high-amplitude waves and will cause individual temperature features along the top intrusion, as discussed below. The first of the two lines enters the intrusion from Fig. 5(d–f) and forms a new temperature feature along the intrusion boundary in Fig. 5(g–i). The second one also enters the intrusion [Fig. 5(e–g)], but due to a temperature gradient between the two it cannot close the gap to the first one. Therefore, it slides above it [Fig. 5(g–i)] forming a second temperature feature. Owing to the many waves coming in from the hot boundary layer, a multiple-line structure similar to the one shown in Fig. 4(e) is finally achieved. These features continue to travel along the intrusion until they disappear, presumably due to dispersion. In the end there are no traces left of them, as shown, e.g. in Fig. 4(k).

3.2. *Discussion*

The sequences shown in Figs. 4 and 5 depict a range of complex interactions between the incoming boundary-layer waves and the established horizontal intrusion flow. Although there are similarities to the interaction of the first group of waves with the developing intrusion as discussed in ref. [9], there are also significant differences. The immediate result of the wave-intrusion interaction is the formation of a layered temperature structure on the lower edge of the intrusion, similar to that observed with the first group of waves. In this case however, the structures are more intense, which is consistent with the higher amplitude of the second wave group (compare Fig. 3 with Fig. 3 of ref. [9]). While for the first group of waves the layered structure is constrained by the presence of the detraining fluid behind the head of the initial intrusion flow, there is no such restriction for the second wave group. Here, the structure appears to slowly move downstream and dissipates before it has reached the mid-point of the cavity. The last remnants are visible in Fig. 4(h), and the effect has vanished in Fig. 4(i).

Figure 5(a–d) shows the shadowgraph image of one individual boundary-layer wave, which consists of two sharp lines of high intensity. As discussed in ref. [9], these lines approximately correspond to regions of high second derivatives of the temperature field in a direction normal to the lines. Therefore, this double-line structure can be interpreted such that the temperature along a horizontal line first decreases from its value at the vertical boundary to some minimum away from the wall, then rises again to a local maximum before it finally decreases to its core value. The isotherms will show a roll-like structure similar to a surface wave about to break, although in this case the open end of the roll is towards the upstream end of the wave. Numerical simulations of the boundary-layer waves at similar Rayleigh numbers have in fact resulted in temperature fields showing this characteristic [see Fig. 1(b) of ref. [7]], thus supporting our interpretation of the images.

Not immediately obvious from Fig. 5 is the fact that the waves travel much faster along the intrusion than along the boundary layer. By tracking the progress of the waves, the respective velocities may be estimated as 4.5 mm s^{-1} on the boundary layer [Fig. 5(c–e)] and 7.2 mm s^{-1} on the intrusion [Fig. 5(e–h)], before they get arrested on the separation region. Watching these waves in real time, either during an experiment or from the recorded videotape, presents a particularly striking representation of this effect, and the change in speed is quite clear. Once on the intrusion, the layered structure, and therefore presumably the roll-like structure, of the temperature field is preserved, although there is clearly increased interaction between successive waves.

The presence of a temperature structure near the top wall has also been observed during the initial intrusion [9]. In that case, the structure had slowly moved down-stream, and has been associated with the flow separation observed at that point. Here, the temperature structure seems to move back upstream, a motion which coincides with the arrival of the second group of waves. Figure 4(a, b) shows the structures essentially stationary, represented by the sharp gradient at about 5 cm downstream from the top left corner. Figure 4(c) shows the arrival of the first boundary-layer wave in the intrusion and the formation of the layered structure on the lower intrusion boundary, as discussed above. At the same time, the gradient at the top boundary has moved back towards the upstream corner and is now less than 4 cm away from the left wall. This process continues as more waves arrive. With the formation of the increasingly complex structure on the lower intrusion edge, the separation structure moves further upstream [Fig. 4(d–g)]. After the last wave interaction has occurred by Fig. 4(h), the separation structure becomes stationary at about 2 cm away from the left wall, however, the flow begins to steepen significantly [Fig. 4(h–k)], and the flow reversal referred to above becomes evident.

The mechanisms responsible for these changes are still not known. It is clear, however, that the passage

of the second group of waves triggers a rather strong response in the essentially steady intrusion, which has formed following the initial start-up flow. In ref. [6], it was suggested that the flow separation was due to the adjustment of the stratified intrusion as it exits from the corner to the different thermal boundary condition at the cavity ceiling. At the top wall, this adjustment effectively leads to a blocking of the fluid coming from the boundary layer, thus forcing the flow to deviate from the horizontal direction (for details see ref. [6]). The presence of the sharp gradient at the horizontal boundary and the coincidence of the steepening of the exiting flow from the corner with the steepening of the intense gradient are consistent with this argument. Following the first flow reversal associated with the separation caused by the blocking at the top wall, the flow reverses again and reattaches to the cavity top. Evidently, this is the result of buoyancy forces, since the intrusion fluid is still relatively less dense than the ambient. There is some indication of a second separation region further downstream, which however is considerably weaker than the first one, thus leading to a correspondingly weaker flow deviation away from the top wall. Throughout the time series shown in Fig. 4, the intrusion fluid coming from the hot boundary layer is warmer than the cavity core which is still isothermal. Therefore, a strong temperature gradient exists between the two regions, which is indicated by the relatively bright line seen in all frames of Figs. 4 and 5 separating the intrusion from the core.

4. EVOLUTION TO THE FINAL STEADY STATE

4.1. *Observations*

For typical temperature differences ΔT of about 2–4 K, the second group of waves has travelled by and disappeared in the intrusion about 2.5–3 min after start-up. Further development then occurs at much longer time scales. In the following, we will describe the approach to a steady-state flow by using two different time series. The first one shown in Fig. 6 visualizes the further evolution of the intrusion flow. This series is again constructed from the same horizontal strip around the top intrusion, but now from a somewhat broader region (≈ 5.9 cm wide) than shown in the previous figures. The time elapsed between consecutive images is 15 s with Fig. 6(a) taken 156 s and Fig. 6(h) 261 s after start-up, so that a range of almost 2 min is covered. With a Rayleigh number of $Ra = 7.3 \times 10^8$, this experiment is very similar to the one used for Fig. 4. Figure 6(a) is taken at about the same time as Fig. 4(k), when the second group of waves has just vanished inside the intrusion.

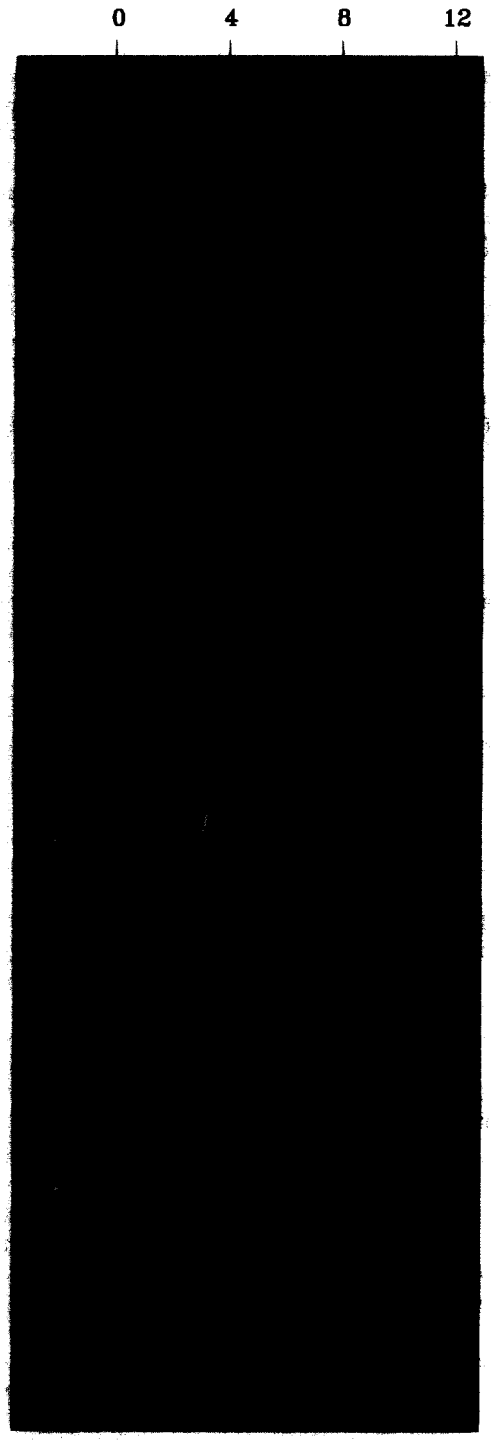

Fig. 6. Time series of shadowgraph images showing the further evolution of the intrusion flow after the second wave group has gone by ($Ra = 7.3 \times 10^8$). The individual parts correspond to the following times after start-up: (a) 156 s, (b) 171 s, (c) 186 s, (d) 201 s, (e) 216 s, (f) 231 s, (g) 246 s, (h) 261 s.

In the subsequent evolution of the intrusion, two different developments can be distinguished. The most striking one probably is the behaviour of the flow-reversal region close to the hot boundary layer. The various up- and downflow regimes with the strong temperature gradients between them come closer together and form a roll-like structure, which approaches the hot wall [Fig. 6(a–d)]. The whole structure then unwraps itself with the upflow part slowly moving downwards and combining with the downflow part

[Fig. 6(e–g)]. Finally, the highly curved nature of this part of the intrusion as shown in Fig. 6(a) has vanished. It seems that the remnant of the intrusion now further approaches the hot boundary layer and will eventually merge into it in order to form the steady-state boundary layer, an assumption which is supported by the observations in Fig. 7. The second characteristic of the intrusion development is the change of the laminar flow behind the flow-reversal region from being well-pronounced in Fig. 6(a) to being barely visible in Fig. 6(h). The strong temperature gradient between the intrusion and the cavity core as shown in Fig. 6(a) weakens and apparently conducts into the cavity. The formerly isothermal core is now slowly being stratified with the stratification coming in from the top and bottom boundaries, i.e. from the respective intrusions.

The final part of the approach to the steady state and especially the evolution of the vertical boundary layer is visualized by the four images of Fig. 7, which are taken from the same experiment as the images used for Fig. 6 ($Ra = 7.3 \times 10^8$). Shown in Fig. 7 are the top 11.9 cm of the cavity at different times. Figure 7(a) is taken 343 s after start-up, i.e. 82 s after Fig. 6(h). The remnant of the intrusion is now much smoother, and the merging of the intrusion into the boundary layer as discussed above is obvious. There is no further sign of the strong vertical temperature gradient between the top boundary and the core region, and the separation region is only weakly evident. The development of the vertical boundary layer continues in Fig. 7(b), which is taken 2 min after Fig. 7(a). The former intrusion now extends further down, with a relatively strong horizontal temperature gradient being established between the boundary layer and the interior of the cavity. This gradient has weakened, although not vanished, in Fig. 7(c) which is taken 12 min after Fig. 7(b). The new feature now extends further downwards than in Fig. 7(b). The last part of this sequence, Fig. 7(d), is taken 56 min after Fig. 7(c), i.e. 70 min after Fig. 7(a), and represents the final steady state. The new shape of the vertical boundary layer now extends right down to the bottom (not shown here), and the gradient towards the interior has further weakened. The bright features at the top of the boundary layer in Fig. 7(d) represent the steady-state waves as referred to in the next section.

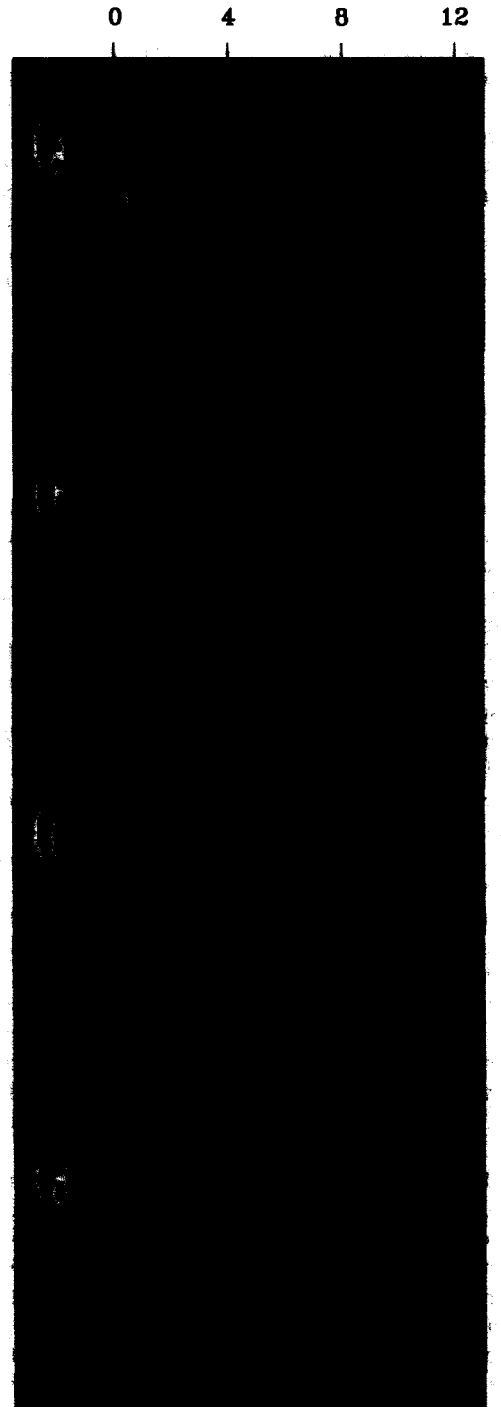

Fig. 7. Shadowgraph images showing the approach to the final steady state ($Ra = 7.3 \times 10^8$). (a) is taken 343s after start-up, (b) 2 min later, (c) another 12 min later and (d) another 56 min later, i.e. 70 min after (a) and approximately 76 min after start-up.

4.2. *Discussion*

A sequence of changes to the structure associated with the complex flow-reversal region near the exit from the vertical boundary layer is shown by Fig. 4(h–k) and Fig. 6. These processes may be loosely described as an upstream motion and a steepening of the flow separation [Fig. 4(h–k)], followed by a more fundamental change when the structure itself appears to unroll, thus dividing the flow into two parts (Fig. 6). One part deviates downwards toward the rising vertical boundary layer, while the other one flows horizontally along the top wall, with continued, but weaker indication of the separation region.

These changes are connected to the equivalent of the 'piling up' of cold fluid from the incoming cold intrusion at the base of the hot boundary layer dis-

cussed in refs. [1, 9] and shown in Fig. 3. As noted in ref. [1], this leads to tilted isotherms and to the generation of internal waves. The first relaxation of the tilt is visible in the second half of Fig. 3. There is a corresponding effect at the upper end of the cold boundary layer resulting from the hot intrusion travelling along the top wall of the cavity. The time scale for these processes is given by the internal-wave period. For the simple model of two horizontal layers of isothermal fluid, this period is given by (see ref. [23]):

$$T = 2h\left(g'\frac{d_1 d_2}{d_1 + d_2}\right)^{-1/2}. \qquad (2)$$

Here, $g' = g\Delta\rho/\rho_0$ is the reduced gravity given by the density difference $\Delta\rho$ between the two layers which have the thicknesses d_1 and d_2, respectively. Although in our case the intrusion is stratified and d_1 (and hence d_2) varies slightly, we may estimate $\Delta T_i \approx 3$ K for the temperature difference between the intrusion and the ambient, and $d_1 \approx 2$ cm and $d_2 \approx 10$ cm. In the last step, we have assumed that half of the cavity height is responsible for the motion under consideration. This yields $g' \approx 62 \times 10^{-4}$m s^{-2} and hence $T \approx 47$ s. The influence of the first relaxation on the upstream end is expected after $T/2 \approx 23.5$ s. From Fig. 3, we can estimate that the relaxation begins at about 114 s after start-up [Fig. 3(n)], therefore the effect should be visible at the flow-reversal structure after about 138 s. The steepening of the structure is first evident in Fig. 4(h), which is taken 141.08 s after start-up, close to the time predicted for the arrival of the signal from the downstream end. Therefore, the steepening is consistent with the adjustment of the non-horizontal temperature isotherms, thus increasing the temperature downstream of the flow-reversal structure and effectively providing additional blocking to the exiting flow.

The second stage of the changes to the flow-reversal structure is the apparent unrolling and splitting as evident in Fig. 6. Through the adjustment of the vertical boundary layer and the stratification of the cavity core, the merging of the structure with the existing boundary layer seems to play an important role in the evolution to the steady state. A detailed account of the first part of this process, based on both experimental and numerical results, was given in ref. [6] at a Rayleigh number of about half the present value. After its impact on the opposite boundary layer, the intrusion flow is divided into two streams with one travelling along the horizontal wall and the other diverging into the core region. This splitting first occurs at the downstream end (i.e. near the opposite vertical wall), and subsequently the point of separation moves back upstream (see Fig. 13 in ref. [6]). Eventually, it reaches the flow-reversal region, which is forced back towards the emergent corner and towards the cavity core. Although at a somewhat higher Rayleigh number, the same mechanism is evidently operating in the present experiments.

The time series of Fig. 6 shows how the flow-reversal region detaches and becomes distinct from the flow exiting into the intrusion, which is again consistent with ref. [1]. This region then appears to merge with the vertical boundary layer. The edge of the existing boundary layer is represented by the bright, almost vertical, line extending upwards from the bottom in Fig. 7(a–c). At a certain point, it reaches the boundary of the detached flow-reversal region, and the merged region is evident above this point. The point of intersection moves upstream (downwards) along the boundary layer through Fig. 7(a–c), and has moved out of view in Fig. 7(d). Downstream (upwards) of the point of intersection, the boundary layer has changed character substantially. Its outer edge is displaced towards the interior of the cavity and the gradients are much weaker than previously. They will however remain, since the interior of the cavity is now almost linearly stratified from bottom to top, while the temperature of the sidewall is constant over its whole length, thus leading to a region of adjustment. The stratification of the interior is also weakly visible in Fig. 7.

During the evolution shown in Fig. 6, the intrusion appears to be periodically disturbed, as can be seen by the multiple-line structures at the bottom boundary of the flow-reversal region in Figs. 6(c and e). These patterns look similar to the splitting structure discussed earlier in Section 3. By inspecting additional frames which have been taken in between the ones shown in Figs. 4 and 6, we can estimate the times for the start and end of these disturbances. The interaction with the second group of waves takes place from about 116 to 146 s after start-up. The first disturbance thereafter arrives at about 176 s and vanishes at about 191 s after start-up, while the second disturbance lasts from 216 to 241 s after start-up. Therefore, we can associate a period of 60–40 s with this feature, which lasts 15–25 s each time. The decrease of the period with higher internal stratification is consistent with previous numerical and experimental investigations [6,7]. There is another, much weaker disturbance following the second one, however, it is not possible to define its temporal boundaries very well, although they seem to be consistent with the above estimates.

One mechanism for these disturbances could be an internal wave motion interacting with the intrusion flow, which has already been considered above in connection with the relaxation of the tilted isotherms. From equation (2), the period of this motion has been estimated to about 47 s, which is in agreement with our measurements. Another possibility is that the disturbance caused by the impact of the second wave group subsequently travels around the cavity before it decays. Even if this process is not strong enough to produce detectable waves along the boundary layers, it may still be able to perturb the flow-reversal region

of the intrusion, which seems to show a strong response to even very small disturbances (see discussion in Section 3). Following the measurements of ref. [9], it will take about 30 s for the travel along the vertical boundary layer, while according to ref. [6] the travel time along the horizontal boundary should be of the same order, although slightly longer. This yields an estimate for the complete time of about 60–70 s, which is in agreement with the arrival for the first disturbance, but seems to be too long to describe the subsequent perturbations. From our measurements it is not possible to determine which, if either, of the processes is responsible for these disturbances.

5. STEADY-STATE BOUNDARY-LAYER WAVES

5.1. *Observations*

The final state is steady in the sense that the flow characteristics averaged over time become constant, although the motion itself may still be time-dependent. In all of our steady-state experiments, we have observed waves travelling continuously along the vertical boundary layer, with amplitude and frequency depending on the temperature difference. Figure 8 is the representation of such a travelling-wave state. Here, the temperature difference is $\Delta T = 3.5$K, corresponding to $Ra = 7.3 \times 10^8$. Similar to Fig. 3, Fig. 8 is again a time series showing the same vertical strip ($\approx$ 1.1 cm wide) around the hot boundary layer. The time elapsed between consecutive images is 2.5 s and the series is taken about 2 days after start-up. Since the motion does not change qualitatively, it is not important to know the exact time elapsed since the flow initiation. Our longest run lasted over many days, still showing the same wave characteristics. From Fig. 8(a–z), 62.5 s of this travelling-wave state are covered. Several individual wave peaks can clearly be distinguished and followed from being hardly visible (about one half to two thirds of the distance up the boundary layer) until they disappear in the hot top corner. During their travel along the boundary layer, their amplitudes increase, indicating that the boundary layer is unstable. In all our experiments, even for the smallest temperature differences ($\Delta T \approx 0.5$K), the final steady state was characterized by such waves. For very small temperature differences, the amplitude was much weaker, but not zero.

5.2. *Discussion*

The locations of the individual wave peaks as extracted from the experiment used to create Fig. 8 are shown as functions of time in Fig. 9. Figure 8 has only covered a representative section of the experiment, which in fact lasted much longer than 62.5 s. It has been recorded for about 130 s and 30 different wave peaks could be identified during that time. The lines in Fig. 9 are approximately parallel, suggesting that the speed is about the same for all the waves.

Fig. 8. Time series of shadowgraph images showing the final steady state for $Ra = 7.3 \times 10^8$. Waves are travelling continuously up the hot boundary layer. The series is taken about 2 days after start-up with 2.5 s elapsed between consecutive images.

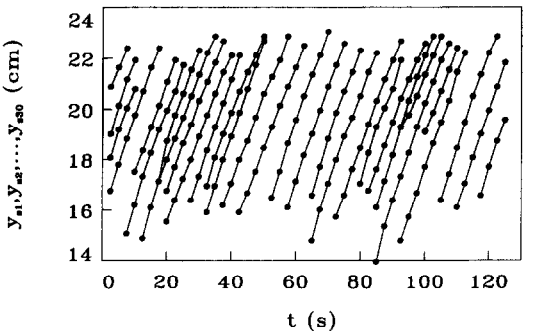

Fig. 9. Locations of individual wave peaks up the hot boundary layer as functions of time for the steady-state waves shown in Fig. 8. The time origin is chosen arbitrarily.

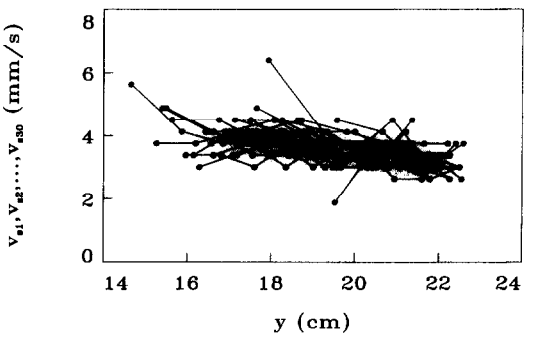

Fig. 10. Velocities of the individual wave peaks of Fig. 9 as functions of the distance up the hot boundary layer.

A preferred distance between the lines can also be recognized, supporting the assumption that the system has an intrinsically preferred frequency. This preference, however, is weak thus allowing the presence of other frequencies, which is also obvious from Fig. 9. Another very interesting feature is the creation and annihilation of waves (those points in Fig. 9 where two lines meet). This mechanism is presumably used to maintain the preferred frequency and will be studied and discussed in more detail in further investigations.

The final Fig. 10 shows the velocities of all the 30 wave peaks included in Fig. 9 as functions of the location up the hot boundary layer. For simplicity, the velocities have been approximated by assuming a constant motion between two data points, thus yielding an estimate for the velocities at intermediate times and locations. Although this gives only a very limited resolution, the general trend is clear. The velocities are approximately the same for all waves observed (as already assumed by inspecting Fig. 9), with an average velocity of about 4 mm s^{-1}. From the current data it is hard to determine whether the slight decrease of the velocity higher up the boundary layer is generic or given by the measurement errors.

Unfortunately, we do not have a theoretical prediction for the steady-state wave velocity for our experimental parameters, however, we can get an estimate. For $Ra = 3 \times 10^8$ and $Pr = 7.5$, a stability analysis of the steady-state boundary layer in the presence of a stratified cavity core gives a velocity of 3 mm s^{-1} for the most amplified travelling-wave component (A.M.H. Brooker, private communication). A stability analysis of a stationary boundary layer with no internal stratification yields at a height of 20 cm for the same parameters a velocity of 6.7 mm s^{-1} and for our parameters 10.4mm s^{-1} [24]. If we assume that the ratio of the velocities with and without stratification is approximately constant over a small range of Rayleigh numbers, we can estimate for our parameters a steady-state wave velocity of about 4.7 mm s^{-1}. This is in good agreement with our measurement of about 4 mm s^{-1}.

The observation of these steady-state waves, even for very small temperature differences, seems to contradict some numerical results, where waves could only be seen for a temperature difference above a critical one [11, 12, 14]. We associate this with the fact that our setup creates potentially large disturbances. The experiment has been designed for investigating the transient behaviour, but not especially for the final steady state. The water in the two reservoirs, which are used to change and maintain the temperatures of the sidewalls, is stirred vigorously by immersion heaters. The resulting strong motion in the reservoirs may lead to a slight random variation of the temperature along the copper plates, which may be enough to trigger these waves. We note, however, that the stirring frequency is very much higher than the frequency observed for the boundary-layer waves, which is therefore assumed to be an intrinsically preferred frequency. We also mention that the numerical simulations have either been carried out with air as the working fluid [11,12], or only for very tall, water-filled cavities [14], which could partly explain this discrepancy. To investigate this feature in more detail, a new tank is planned, which will be used especially to study the steady state. In this new tank, the temperatures of the sidewalls are maintained in a different way leading to much less variation and disturbances. The new setup, however, is only suitable for the final steady state, but cannot be used to follow the initial flow evolution.

6. CONCLUSIONS AND OUTLOOK

For the fluid flow in a differentially heated and cooled square cavity, sequences of shadowgraph images have been used to visualize the initial flow development. The experiments are directed at providing the details of the boundary-layer properties following the start-up and the impact of the first intrusion, as well as the approach to the final steady state. The first, fast developing, part of the flow was reported in ref. [9], while the present publication covers the much slower evolution to steady state. This stage is characterized by the interaction of the second group of waves with the intrusion, and by the sub-

sequent development of the stratified cavity core and of the final vertical boundary layer.

Central to the flow development at this stage is the formation and the subsequent collapse of a region of several flow reversals near the upstream end of the horizontal intrusion flow. The mechanisms triggering this flow structure are not fully understood. The observations of the temperature field in this region are however consistent with the interpretation given in ref. [6], that a blocking flow is set up by the change in the boundary conditions for the temperature as the flow exits from the vertical boundary layer into the intrusion. Other models have also been advanced (see e.g. refs. [3, 17]), but it is not clear which, if any, of these is responsible for the behaviour. The adjustment of the vertical boundary layer to its wider steady-state form showing a smaller gradient towards the cavity core is achieved by the merging of the flow-reversal structure into the existing boundary layer. During this process, the structure is forced upstream towards the vertical wall by the internal-wave motion generated by the interaction of the intrusion with the far wall. The flow-reversal structure has a sudden and relatively strong response to the waves coming from the vertical boundary layer, however, it appears that the contraction and upstream motion of the structure is not related to the presence of the waves, although these events occur at approximately the same time.

Although the details of these interactions are not known in a quantitative sense, the interactions have now been demonstrated both numerically and experimentally over a range of Rayleigh numbers. The resulting flows are rather complex, especially in the corner regions with clearly nonlinear interactions. However, the observations are completely reproducible, and there is no suggestion of a transition to turbulence. Many of the results reported here have not been observed previously in the detail available with the shadowgraph technique, particularly with respect to the interactions of the boundary layer waves with the intrusion flow. An understanding of the mechanisms responsible for the formation of the flow-reversal structure near the upstream end of the developing and of the established intrusions is of particular importance, as it is this structure and its interaction with the other flow features which apparently controls the development to the steady-state flow. A numerical and analytical investigation of these processes is currently under way.

Acknowledgements—Useful discussions with Andrew Brooker and Tasman Graham are gratefully acknowledged. This research was supported by the Australian Research Council under grants A89231072 and A89331991. WS is the recipient of a University Postdoctoral Research Fellowship by the University of Western Australia.

REFERENCES

1. J. Patterson and J. Imberger, Unsteady natural convection in a rectangular cavity, *J. Fluid Mech.* **100,** 65–86 (1980).
2. R. Yewell, D. Poulikakos and A. Bejan, Transient natural convection experiments in shallow enclosures, *ASME J. Heat Transfer* **104,** 533–538 (1982).
3. G. N. Ivey, Experiments on transient natural convection in a cavity, *J. Fluid Mech.* **144,** 389–401 (1984).
4. S. G. Schladow, J. C. Patterson and R. L. Street, Transient flow in a side-heated cavity at high Rayleigh number: a numerical study, *J. Fluid Mech.* **200,** 121–148 (1989).
5. S. G. Schladow, Oscillatory motion in a side-heated cavity, *J. Fluid Mech.* **213,** 589–610 (1990).
6. J. C. Patterson and S. W. Armfield, Transient features of natural convection in a cavity, *J. Fluid Mech.* **219,** 469–497 (1990).
7. S. W. Armfield and J. C. Patterson, Direct simulation of wave interactions in unsteady natural convection in a cavity, *Int. J. Heat Mass Transfer* **34,** 929–940 (1991).
8. C. G. Jeevaraj and J. C. Patterson, Experimental study of transient natural convection of glycerol–water mixtures in a side heated cavity, *Int. J. Heat Mass Transfer* **35,** 1573–1587 (1992).
9. W. Schöpf and J. C. Patterson, Natural convection in a side-heated cavity: visualization of the initial flow features, *J. Fluid Mech.* **295,** 357–379 (1995).
10. D. G. Briggs and D. N. Jones, Two-dimensional periodic natural convection in a rectangular enclosure of aspect ratio one, *ASME J. Heat Transfer* **107,** 850–854 (1985).
11. P. Le Quéré and F. Penot, Numerical and experimental investigation of the transition to unsteady natural convection of air in a vertical differentially heated cavity, *ASME Heat Transfer Div.* **94,** 75–82 (1987).
12. S. Paolucci and D. R. Chenoweth, Transition to chaos in a differentially heated cavity, *J. Fluid Mech.* **201,** 379–410 (1989).
13. R. A. W. M. Henkes and C. J. Hoogendoorn, On the stability of natural-convection flow in a cavity heated from the side, *Appl. Sci. Res.* **47,** 195–220 (1990).
14. P. Le Quéré, Transition to unsteady natural convection in a tall water-filled cavity, *Phys. Fluids A* **2,** 503–515 (1990).
15. R. J. A. Janssen, R. A. W. M. Henkes and C. J. Hoogendoorn, Transition to time-periodicity of a natural-convection flow in a 3D differentially heated cavity, *Int. J. Heat Mass Transfer* **36,** 2927–2940 (1993).
16. S. W. Armfield and J. C. Patterson, Wave properties of natural-convection boundary layers, *J. Fluid Mech.* **239,** 195–211 (1992).
17. M. R. Ravi, R. A. W. M. Henkes and C. J. Hoogendoorn, On the high-Rayleigh-number structure of steady laminar natural-convection flow in a square enclosure, *J. Fluid Mech.* **262,** 325–351 (1994).
18. J. E. Simpson, *Gravity Currents: In the Environment and the Laboratory* (1st Edn), p. 141. Ellis Horwood, Chichester (1987).
19. W. Merzkirch, *Flow Visualization* (1st Edn), p. 62. Academic, New York (1974).
20. S. Rasenat, G. Hartung, B. L. Winkler and I. Rehberg, The shadowgraph method in convection experiments, *Exp. Fluids* **7,** 412–419 (1989).
21. B. L. Winkler and P. Kolodner, Measurements of the concentration field in nonlinear travelling-wave convection, *J. Fluid Mech.* **240,** 31–58 (1992).
22. W. Schöpf and I. Rehberg, The influence of thermal noise on the onset of travelling-wave convection in binary fluid mixtures: an experimental investigation, *J. Fluid Mech.* **271,** 235–265 (1994).
23. J. S. Turner, *Buoyancy Effects in Fluids*, p. 20. Cambridge University Press, Cambridge (1973).
24. A. M. H. Brooker, The properties of transient instabilities in a boundary layer, *Proc. Fourth Australian Natural Convection Workshop*, Perth, 1–3 December. Report no. ED 834—Centre for Water Research, University of Western Australia (1993).